Supplement of Atmos. Chem. Phys., 25, 7299–7313, 2025
https://doi.org/10.5194/acp-25-7299-2025-supplement

Atmospheric Chemistry and Physics
Open Access

Supplement of

Observational constraints suggest a smaller effective radiative forcing from aerosol–cloud interactions

Chanyoung Park et al.

Correspondence to: Chanyoung Park (chanyoung.park@miami.edu)

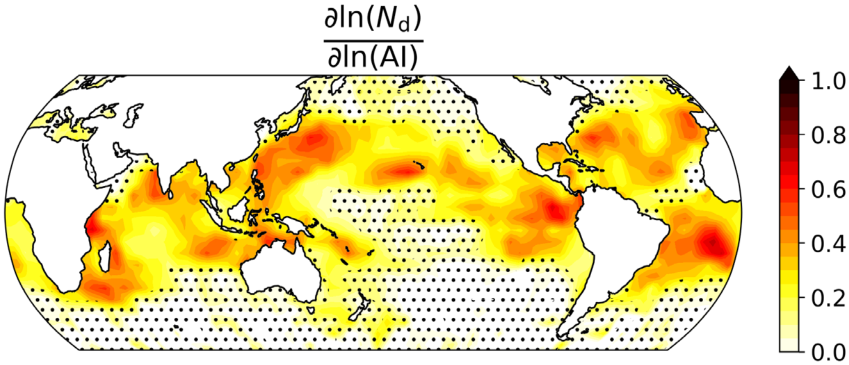

Figure S1. Regression coefficient map of the activation rate of cloud droplet number concentration (N_d) in response to variations in aerosol index (AI) for the period January 2003 to December 2019, derived from cloud controlling factor (CCF) analysis (Appendix A6). The color scale indicates the magnitude of sensitivity, where an increase in AI corresponds to an increase in N_d. Areas with stippling indicate where the changes are not statistically different from zero at the 95% confidence level using Student's t test.

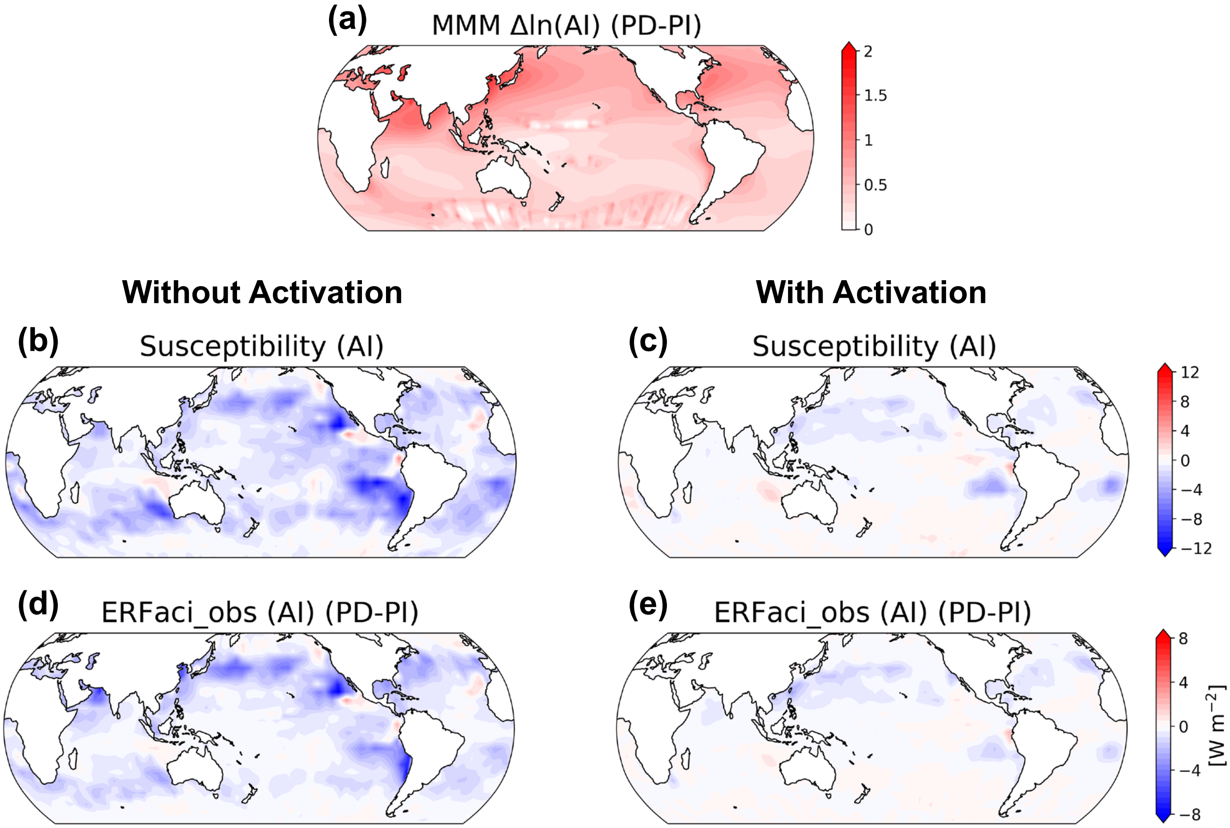

Figure S2. Spatial distribution of ERFaci_obs components and the estimated ERFaci_obs differentiated by the consideration of the activation rate. (a) Multi-model mean (MMM) of changes in AI between pre-industrial (PI) and present-day (PD) periods. 9 models are used for this analysis (Table S1). (b,c) Susceptibility of low cloud radiative effect to AI derived from CCF analysis using observational and reanalysis data (Appendix A6). (d,e) Observationally constrained ERFaci for AI estimated by multiplying the susceptibility with the changes in AI.

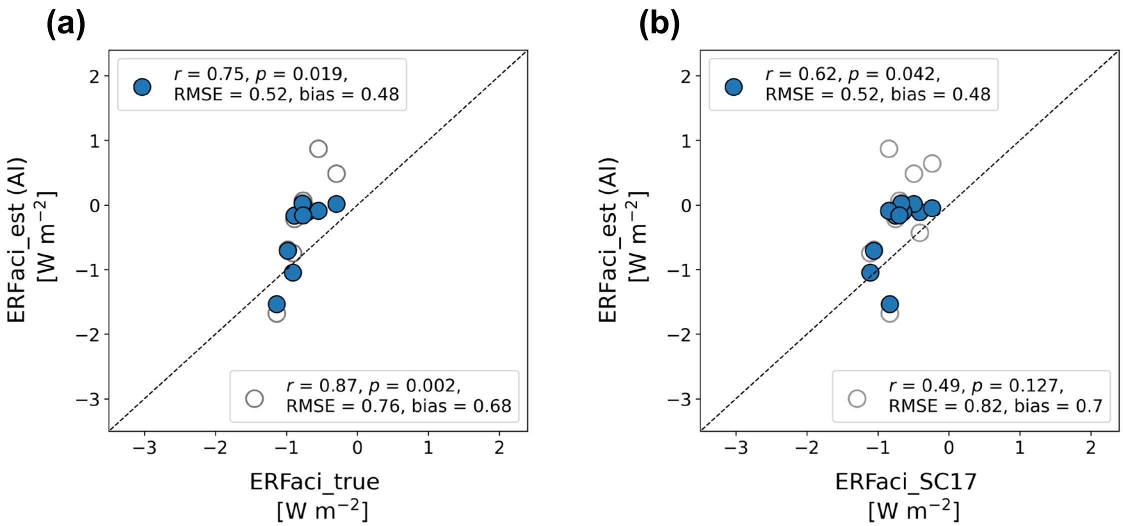

Figure S3. "Perfect-model" cross validation analysis of global-mean ERFaci estimates. (a) ERFaci_true versus ERFaci_est which is estimated by simplified version of Eq. (1) and Eq. (2) with AI as the aerosol proxy instead of SO_4^{2-} (Appendix A7), and (b) ERFaci estimates obtained using the method proposed by Soden and Chung (2017; SC17) versus ERFaci_est. Filled blue circles represent estimates where the activation rate is considered, and open grey circles represent estimates without activation rate consideration. The correlation coefficient (*r*), associated *p*-value (*p*), Root Mean Square Error (RMSE), and bias are displayed in the upper left corner for the filled blue circles and in the lower right for the open grey circles in each panel. Bias is defined as the mean absolute difference from the 1:1 reference line, depicted by a dashed line. All panels have identical x and y axis ranges to highlight the variance among the estimation methods. Higher *r* values, lower RMSE, and minimal bias indicate consistency in ERFaci estimates across different estimation methods using CMIP6 models.

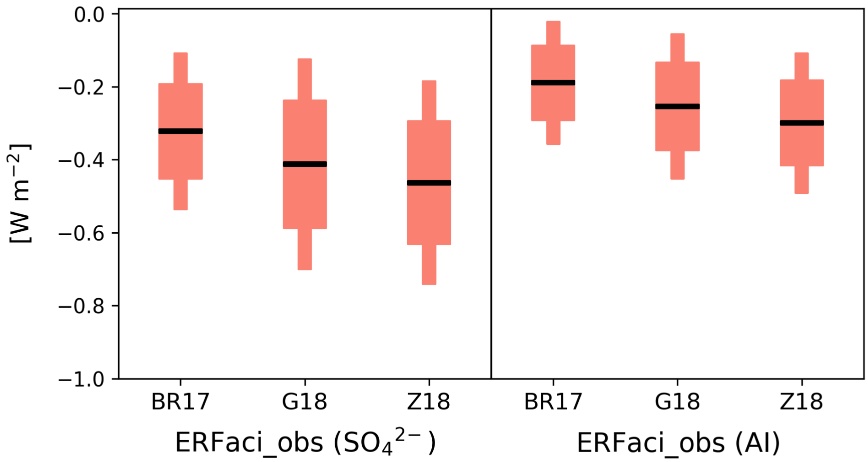

Figure S4. Global ERFaci_obs estimates using three different N_d filtering methods introduced by Gryspeerdt et al. (2022). The left panel shows ERFaci_obs for SO_4^{2-} and the right panel shows ERFaci_obs for AI. BR17 represents global ERFaci_obs estimates based on the filtering method from Bennartz and Rausch (2017), which is used in our study. G18 corresponds to estimates using the filtering method from Grosvenor et al. (2018), and Z18 represents those based on Zhu et al. (2018). Thin and thick bars represent the 90% and 66% confidence intervals (CI), respectively, while the black horizontal lines indicate the best estimate of each ERFaci.

Table S1. CMIP6 models used in the analysis are represented, with each circle indicating the availability of data for a given model. $\Delta\ln(SO_4^{2-})$ and $\Delta\ln(AI)$ represent changes in sulfate mass concentration and aerosol index, respectively, from present day to pre-industrial levels on a natural logarithmic scale. ERFaci_true refers to ERFaci derived from single-forcing (aerosol-only) experiments, while ERFaci_SC17 is calculated using the method from Soden and Chung (2017). ERFaci_est (SO_4^{2-}) and ERFaci_est (AI) denote estimated ERFaci values based on simplified version of Eq. (1) and Eq. (2) in the CMIP6 models (Appendix A7). The GOOD HIST index represents the absolute difference in global-mean historical warming compared to observations (Appendix A4).

	Model	Δln(SO_4^{2-})	Δln(AI)	ERFaci_true	ERFaci_SC17	ERFaci_est (SO_4^{2-})	ERFaci_est (AI)	GOOD HIST index
1	ACCESS-CM2			o	o			0.323
2	ACCESS-ESM1-5			o	o			0.184
3	AWI-CM-1-1-MR				o			0.074
4	AWI-ESM-1-1-LR				o			0.141
5	BCC-CSM2-MR				o			0.319
6	BCC-ESM1	o		o	o	o		0.448
7	CAMS-CSM1-0				o			0.268
8	CanESM5			o	o			0.169
9	CanESM5-1				o			0.248
10	CanESM5-CanOE				o			0.306
11	CAS-ESM2-0				o			0.366
12	CESM2			o	o			0.147
13	CESM2-FV2				o			0.288
14	CESM2-WACCM				o	o		0.104
15	CESM2-WACCM-FV2				o			0.372
16	CIESM				o			0.212
17	CMCC-CM2-SR5				o			0.173
18	CMCC-ESM2				o			0.165
19	CNRM-CM6-1			o	o			0.029
20	CNRM-CM6-1-HR				o			0.014
21	CNRM-ESM2-1	o		o	o	o	o	0.191
22	E3SM-1-0				o			0.289
23	E3SM-2-0				o			0.749
24	EC-Earth3			o	o			0.136
25	EC-Earth3-AerChem	o	o	o	o	o	o	0.362
26	EC-Earth3-CC				o			0.503
27	EC-Earth3-Veg				o			0.153
28	EC-Earth3-Veg-LR				o			0.127
29	FGOALS-f3-L				o			0.115
30	FIO-ESM-2-0				o			0.256
31	GFDL-CM4	o		o	o	o		0.242
32	GFDL-ESM4	o	o	o	o	o	o	0.43
33	GISS-E2-1-G			o	o			0.347
34	GISS-E2-1-H				o			0.115
35	GISS-E2-2-G				o			0.272
36	GISS-E2-2-H				o			0.115
37	HadGEM3-GC31-LL	o	o	o	o	o	o	0.191
38	HadGEM3-GC31-MM				o			0.284
39	ICON-ESM-LR				o			0.287
40	INM-CM4-8				o			0.134
41	INM-CM5-0				o			0.201
42	IPSL-CM5A2-INCA				o			0.293
43	IPSL-CM6A-LR			o	o		o	0.157
44	IPSL-CM6A-LR-INCA	o		o				0.081
45	KACE-1-0-G				o			0.147
46	KIOST-ESM				o			0.15
47	MIROC6	o	o	o	o	o	o	0.327
48	MIROC-ES2L				o	o		0.296
49	MPI-ESM1-2-HR				o			0.15
50	MPI-ESM1-2-LR				o			0.072
51	MPI-ESM-1-2-HAM	o	o	o	o	o	o	0.507
52	MRI-ESM2-0	o	o	o	o	o	o	0.329
53	NESM3				o			0.216
54	NorCPM1				o			0.17
55	NorESM2-LM	o	o	o	o	o	o	0.455
56	NorESM2-MM	o	o	o	o	o	o	0.366
57	SAM0-UNICON				o			0.362
58	TaiESM1				o			0.417
59	UKESM1-0-LL	o	o	o	o	o	o	0.325
60	UKESM1-1-LL				o			0.098

References

Bennartz, R. and Rausch, J.: Global and regional estimates of warm cloud droplet number concentration based on 13 years of AQUA-MODIS observations, Atmospheric Chemistry and Physics, 17, 9815–9836, https://doi.org/10.5194/acp-17-9815-2017, 2017.

Grosvenor, D. P., Sourdeval, O., Zuidema, P., Ackerman, A., Alexandrov, M. D., Bennartz, R., Boers, R., Cairns, B., Chiu, J. C., Christensen, M., Deneke, H., Diamond, M., Feingold, G., Fridlind, A., Hünerbein, A., Knist, C., Kollias, P., Marshak, A., McCoy, D., Merk, D., Painemal, D., Rausch, J., Rosenfeld, D., Russchenberg, H., Seifert, P., Sinclair, K., Stier, P., van Diedenhoven, B., Wendisch, M., Werner, F., Wood, R., Zhang, Z., and Quaas, J.: Remote Sensing of Droplet Number Concentration in Warm Clouds: A Review of the Current State of Knowledge and Perspectives, Reviews of Geophysics, 56, 409–453, https://doi.org/10.1029/2017RG000593, 2018.

Gryspeerdt, E., McCoy, D. T., Crosbie, E., Moore, R. H., Nott, G. J., Painemal, D., Small-Griswold, J., Sorooshian, A., and Ziemba, L.: The impact of sampling strategy on the cloud droplet number concentration estimated from satellite data, Atmospheric Measurement Techniques, 15, 3875–3892, https://doi.org/10.5194/amt-15-3875-2022, 2022.

Soden, B. and Chung, E.-S.: The Large-Scale Dynamical Response of Clouds to Aerosol Forcing, Journal of Climate, 30, 8783–8794, https://doi.org/10.1175/JCLI-D-17-0050.1, 2017.

Zhu, Y., Rosenfeld, D., and Li, Z.: Under What Conditions Can We Trust Retrieved Cloud Drop Concentrations in Broken Marine Stratocumulus?, Journal of Geophysical Research: Atmospheres, 123, 8754–8767, https://doi.org/10.1029/2017JD028083, 2018.